

# Rapid, robust, and automated mapping of tidal flats in China using time series Sentinel-2 images and Google Earth Engine



Mingming Jia<sup>a</sup>, Zongming Wang<sup>a,d,\*</sup>, Dehua Mao<sup>a</sup>, Chunying Ren<sup>a</sup>, Chao Wang<sup>b</sup>, Yeqiao Wang<sup>c,\*</sup>

<sup>a</sup> Key Laboratory of Wetland Ecology and Environment, Northeast Institute of Geography and Agroecology, Chinese Academy of Sciences, Changchun 130102, China

<sup>b</sup> State Key Laboratory of Information Engineering in Surveying, Mapping and Remote Sensing, Wuhan University, No.129 Luoyu Road, Wuhan 430079, China

<sup>c</sup> Department of Natural Resources Sciences, University of Rhode Island, Kingston, RI 02881, USA

<sup>d</sup> National Earth System Science Data Center of China, Beijing 100101, China

## ARTICLE INFO

### Keywords:

Tidal flat  
Sentinel-2 imagery  
Maximum spectral index composite (MSIC)  
Otsu algorithm (OA)  
Google Earth Engine  
Edge-points reference  
China

## ABSTRACT

Tidal flats are threatened by tidal reclamation and climatic changes around the world. Particular challenges exist in China where tidal flats are changing rapidly along with accelerated economic development in coastal regions. The unique and important ecosystem functions and services that tidal flats provide in coastal regions warrant the necessary of mapping such a particular land cover type in high precision and accuracy. Existing national tidal flat maps of China, which were derived from the 30-m resolution Landsat imagery and auxiliary data, are insufficient to support practical management efforts. In this study, in order to produce an accurate tidal flat map with finer spatial resolution, we employed 28,367 scenes of time series Sentinel-2 images acquired in 2019 and 2020 along the entire coastal line of China. The short revisit cycle (2–5 days) of the Sentinel-2 improved the opportunities of obtaining the highest and lowest tide images, and the finer spatial resolution (10-m) enhanced the capacity of precision tidal flat extraction. A rapid, robust, and automated tidal flat mapping approach is essential to large-scale applications. In this study, we developed an approach by integrating the maximum spectral index composite (MSIC) and the Otsu algorithm (OA), and so named MSIC-OA. By GEE platform, we automated the execution of MSIC-OA to Sentinel-2 images, and produced an up-to-date 10-m spatial resolution tidal flat map of China (China\_Tidal Flat, CTF). Validated by massive field-based observations and selected edge-points, the CTF map achieved an overall accuracy of 95% and the F1 score of 0.93. As we calculated, the total area of tidal flats in China was 858,784 ha, and Jiangsu Province accounted the largest proportion (24%) of the national total. This study is the first attempt to delineate tidal flats automatically at a 10-m spatial resolution. The CTF map can provide essential information for management of coastal ecosystems and facilitate the implementations of coastal and marine related Sustainable Development Goals.

## 1. Introduction

Tidal flats, including intertidal mudflats, rocks, and sands, are transition zones between marine and terrestrial environments (Murray et al. 2012; Wang et al., 2020a). They provide unique ecosystem services, for instance, defending against storm surge, maintaining shoreline, filtering pollutant, and promoting carbon storage (Barbier et al. 2008; Deegan et al., 2000). They also serve as feeding grounds for migrating birds, spawning and nursery habitats for fishes and other marine wildlife (Dhanjal-Adams et al. 2016; Ghosh et al. 2016). However, as one of the most ecologically and economically important ecosystems, tidal flats are

vulnerable in the world (Mitch and Gosselink 2007; Tiner 2013). They are highly threatened by tidal reclamation and natural disturbances (Murray et al. 2015). Sustainable management of coastal tidal flats has been listed in the Sustainable Development Goals (SDGs) of the UN's Agenda 2030 (United Nations, 2015). The unique and important ecosystem functions and services that tidal flats provide in coastal regions warrant the necessary of mapping such a particular land cover type in high precision and accuracy, in order to provide essential information toward coastal management and facilitate the implementation of SDGs.

Coastal tidal flats in China are threatened by noticeable

\* Corresponding authors.

E-mail addresses: [zongmingwang@iga.ac.cn](mailto:zongmingwang@iga.ac.cn) (Z. Wang), [yqwang@uri.edu](mailto:yqwang@uri.edu) (Y. Wang).

industrialization, urbanization, and aquaculture expansion in the past four decades (Hou et al. 2016; Mao et al. 2018; Xu and Gong 2018). Currently, more than 70% of China's medium-to-large cities are located along the coastal zone, which produces over 60% of the national gross domestic product and contributes to 61.5% of the world's aquaculture production (FAO 2016; Ren et al. 2019). More than two-thirds of China's coastlines have been converted into artificial seawalls that caused a series of damages to tidal flats (Ma et al. 2014). Chinese government has exerted enormous efforts to restore and manage the degrading coastal ecosystems in order to achieve the SDGs that related to sustainable management of coastal resources, (Guo et al. 2019; Jiang et al. 2019). Nevertheless, tidal flats reclamation is a key source to bring enormous economic benefits to local communities (Meng et al. 2017). Thus, sustainable strategies are urgently needed for balancing coastal protection and utilization. A reliable and up-to-date national tidal flat map is vital for formulating and implementing the strategies of coastal protections.

Remote sensing has long been used to map intertidal zones. The greatest challenge of such attempts is the variation of tidal inundations. Local-scale mapping efforts usually rely on high spatial resolution images. Topobathymetric LiDAR and field measurements from tide stations, for example, have been reported (Campbell and Wang 2018, 2019). However, due to data availability, these approaches would be difficult to be applied to large areas. With increased capacities in image acquisition, storage, and computing power, studies have been reported in mapping tidal flats over large areas, such as in coastal Australia (Dhanjal-Adams et al. 2016; Sagar et al. 2017), as well as at continental and global scales (Murray et al. 2014; Murray et al. 2019). Generally, methodologies of tidal flat mapping derived from optical imagery can be divided into three approaches, including tide model or terrain-based (Murray et al. 2012; Han et al. 2019), training sample-based machine learning (Zhang et al., 2013; Zhang et al. 2019), and knowledge-based decision tree (Wang et al., 2020a; Wang et al., 2020b).

For the tide model or terrain-based approaches, coastal terrain (DEM) and the waterline of the captured image were combined to simulate the spatial extent of intertidal zones and delineate tidal flats (Cao et al. 2020; Han et al. 2019). Murray et al. (2014) tracked losses of tidal wetlands in the Yellow Sea using Oregon State University China Sea tide model and all available Landsat Archive images. Han et al. (2019) monitored China intertidal zone changes during 1995–2015 based on tidal correction model. However, due to the scarcity of intertidal DEMs, the complexity of coastal topography and spatial variation of tide levels, such approaches induced high uncertainties in large area applications (Zhao et al. 2020b). For training sample-based machine learning approaches, random forest (Zhang et al. 2019) and support vector machine algorithms (Zhang et al., 2013) have been used in classifying tidal flats. These classifications depended on a large number of training samples which were usually laborious and costly to achieve. Meanwhile, in machine learning classification maps, large areas of inland features, such as aquaculture ponds and mudflats, often were misclassified to tidal flats (Murray et al. 2019). For knowledge-based decision tree approaches, multiple studies have been reported in mapping of tidal flats (Wang et al., 2020a; Wang et al., 2020b). These studies extracted tidal flats by universal thresholds derived from empirical knowledge. However, due to the complexity in geographic heterogeneity, the universal thresholds may not be applicable over large areas. Likewise, the decision tree method also misclassified inland features to tidal flats (Wang et al., 2020b). Overall, the existing efforts on mapping large-scale tidal flats relied on either auxiliary data, such as tide level, DEM, and training samples, or manual intervened thresholds, or pre- and post-processing. A rapid, robust, and fully automated approach that based on massive collection of time series remote sensing images is in demand.

To date, Landsat series imagery is the most widely used data for mapping large-scale coastal land covers. For example, a recent study implemented Landsat time series on salt marsh mapping along the Mid-Atlantic coast (Campbell and Wang 2020). However, Landsat images have several shortcomings on mapping tidal flats. First, because of the

frequent clouds of coastal zones and the continuous changing tide levels, it is difficult to obtain high-quality images at the time with the lowest and highest tides given Landsat's temporal resolution of 8–16 days by combining Landsat 7 and 8, especially over large areas. Second, tidal flats always appear in narrow and patchy patterns along the coasts. Smaller patches of tidal flats might not be accurately extracted by Landsat imagery with a 30-m spatial resolution. The free accessibility of the complete archive of 10-m resolution Sentinel-1/2 images and the computing capability provided by Google Earth Engine (GEE, <https://earthengine.google.com>) promoted large-scale remote sensing researches (Gong et al. 2019; Tragano et al. 2018). In particular, the dense temporal resolution of Sentinel-2 images with revisit interval of 2–5 days offers a great opportunity to capture the lowest and highest tides, which is vital to conduct accurate and robust delineation of tidal flats. Combining Sentinel-2 images and the GEE platform made it possible to develop an accurate tidal flat map with more spatial details and up-to-date information. Although several local-scale tidal flats studies used Sentinel-2 imagery (e.g., Gong et al. 2020; Khan et al. 2019), applications toward coverage of extensive areas need to be explored for supporting increased requirements of practical management and conservation efforts.

To address the above-mentioned issues, this study aims to (1) develop a rapid, robust, and automated approach for mapping tidal flat based on the time series Sentinel-2 imagery; (2) apply the approach on the GEE platform to produce an up-to-date 10-m spatial resolution tidal flat map of China, so named China\_Tidal Flat (CTF); (3) evaluate the accuracy of the CTF map by comprehensive validation with massive field-based observations and selected edge-points based on tide station measurements; and (4) analyze the geographical characteristics of tidal flats in China and the potential use of the CTF map.

## 2. Materials and methods

### 2.1. Study area

As illustrated in Fig. 1, coastal zone of China spans more than 20 latitudes ( $18^{\circ}\text{N}$  to  $41^{\circ}\text{N}$ ) and encompasses 12 provinces. The extensive coastal regions from north to south have mean annual temperature and precipitation varying from 5 to  $26^{\circ}\text{C}$  and 400 to 1800 mm (Mao et al. 2019), respectively. Tides across the study area varied in types, including regular and irregular semi-diurnal and diurnal tides. The main landscapes in the intertidal zone of China are tidal flat, mangrove forest, salt marsh, aquaculture pond, built-up land, and water. Along the coastline of China, there are 157 rivers/channels discharging into the sea (general information is listed in the supplementary data).

### 2.2. Basic consideration

In this study, coastal tidal flats were defined as non-vegetated areas between the maximal and minimal tidal inundations, i.e., the highest and lowest tidal waterlines, along the shoreline (Wang et al., 2020a). Thus, to map tidal flats, the key is to obtain spatial distributions of the maximal and minimal water extents between the highest and lowest tides, respectively. To accomplish this, firstly, we synthesized the highest and lowest tide images from the time series Sentinel-2 image collection. Secondly, we created binary classification results, i.e., water and non-water, automatically from the highest and lowest tide images to derive the maximal and minimal water extents, respectively. Thirdly, we intersected the maximal and minimal water extents to obtain intertidal zones. Finally, we removed intertidal vegetation and permanent seawater from the intertidal zones and remained only the areas of tidal flats. The workflow of tidal flat mapping is shown in Fig. 2A. To further explain the workflow, we chose Inner-deep Bay as a case study area (Fig. 2a-f). For more detailed explanations please see Section 2.5.4.



Fig. 1. Location of China's coastal zone and spatial distributions of estuaries and tide types.

### 2.3. Sentinel-2 imagery and pre-processing

The full Sentinel-2 mission comprises twin polar-orbiting satellites (Sentinel-2A launched in June 2015 and Sentinel-2B commissioned in July 2017) in the same orbit. The mission has a wide swath width and short revisit cycle (2–5 days). Both Sentinel-2A and Sentinel-2B carries the state-of-the-art MultiSpectral Instrument sensor that offers 13 spectral bands, with four bands at 10-m (Bands 2, 3, 4, and 8), six bands

at 20-m (Bands 5, 6, 7, 8A, 11, and 12), and three bands at 60-m (Bands 1, 9, and 10) spatial resolutions. All the Sentinel-2 data used in this study are Level-2A products, which means per-pixel radiometric measurements are provided in surface reflectance with all parameters to transform them into radiances. To build a high-quality dense time series image collection, we conducted two procedures.

First, the 28,367 scenes of surface reflectance images covering the entire coasts of China with acquisition dates between January 1, 2019

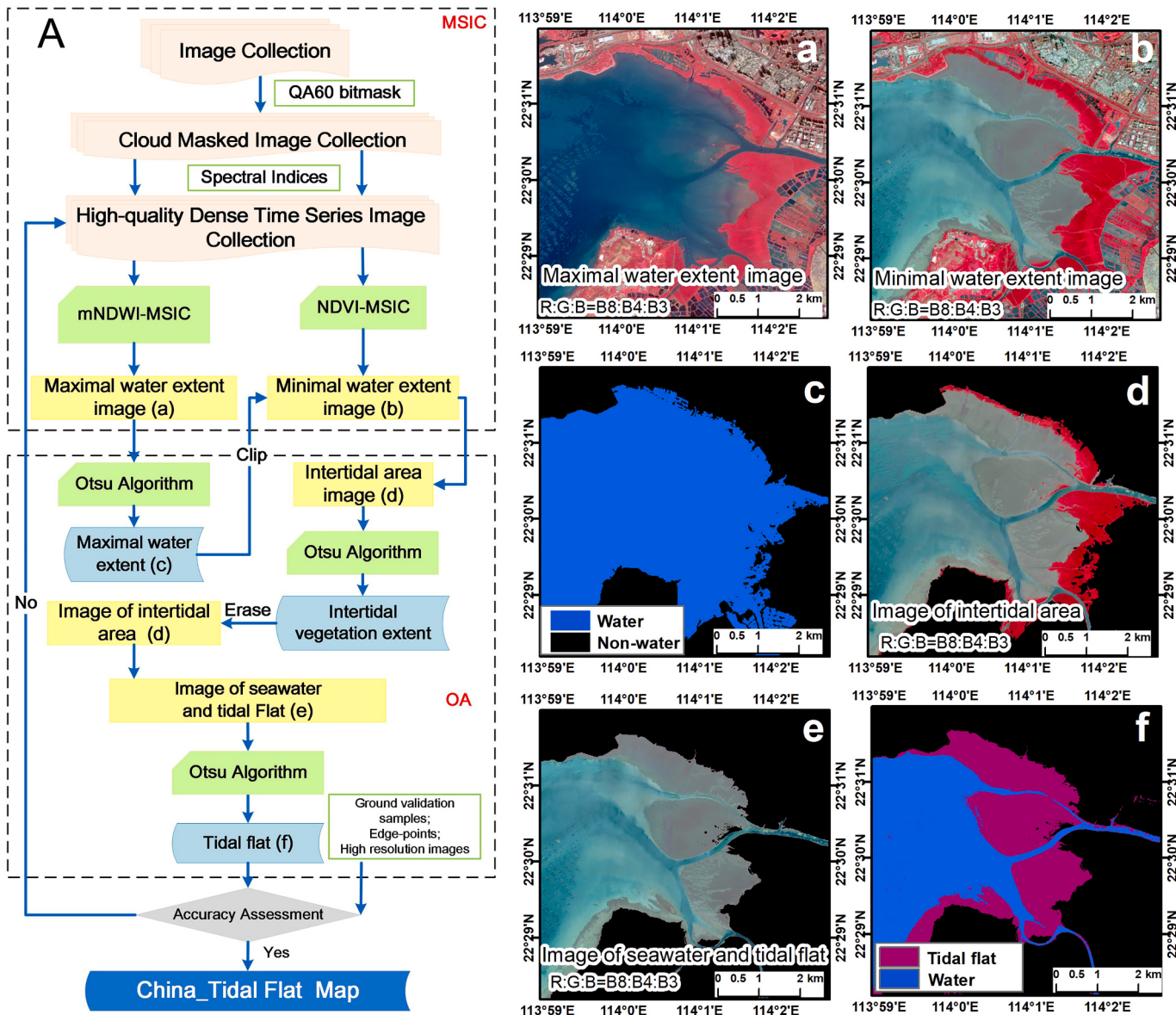


**Fig. 2.** Workflow of tidal flat mapping and results of each step during applying the MSIC-OA to time series Sentinel-2 images of the Inner-deep Bay. (A) Workflow of the MSIC-OA approach. (a-f) Results of each step during delineating tidal flats in the Inner-deep Bay based on the MSIC-OA approach and time series Sentinel-2 images.

and June 30, 2020 were used to build an initial time series image collection. The QA60 bitmask band, which contains cloud information, was used to mask out bad-quality observations caused by opaque and cirrus clouds in each image (Li et al. 2019). The remaining pixels were reserved as good-quality observations. The number of good-quality observations in each location of an individual pixel is referred as good-quality observation number. Spatial distributions and histograms of good-quality observation number for each individual pixel are shown in Fig. 3A and a, respectively. Over 75% of the individual pixels have more than 60 good-quality observations.

Second, five spectral indices were calculated and inserted into each image of the time series image collection. Table 1 shows a list of the indices, including the Nominalized Difference Vegetation Index (NDVI) (Tucker 1979), Enhanced Vegetation Index (EVI) (Huete et al. 1997), Normalized Difference Water Index (NDWI) (McFeeters 1996), modified Normalized Difference Water Index (mNDWI) (Xu 2006), and Normalized Difference Soil Index (NDSI) (Rogers and Kearney 2003). The new image collection was referred as high-quality dense time series image

collection. All the pre-processing tasks of building the collection were conducted in the GEE platform.

#### 2.4. Reference data collection

##### 2.4.1. Ground validation samples

We conducted a series of ground surveys with unmanned aerial vehicle (UAV platform: DJI Phantom 4 pro) flights during 2018 and 2019. Field photos and corresponding locations were taken using a digital camera and geographic positioning system (GPS). The UAV flights were conducted during local lowest tide conditions to detect the tidal flat patches far away from shorelines. The high spatial resolution images accessible in Google Earth were also referenced with ground survey. Fig. 3b shows an example of true-colour UAV image with a spatial resolution of 5 cm, while Fig. 3c and d show examples of field photos recorded in the ground survey.

We used the stratified random sampling approach in selecting validation samples (Chen et al. 2017; Dong et al. 2016; Wang et al., 2020a;

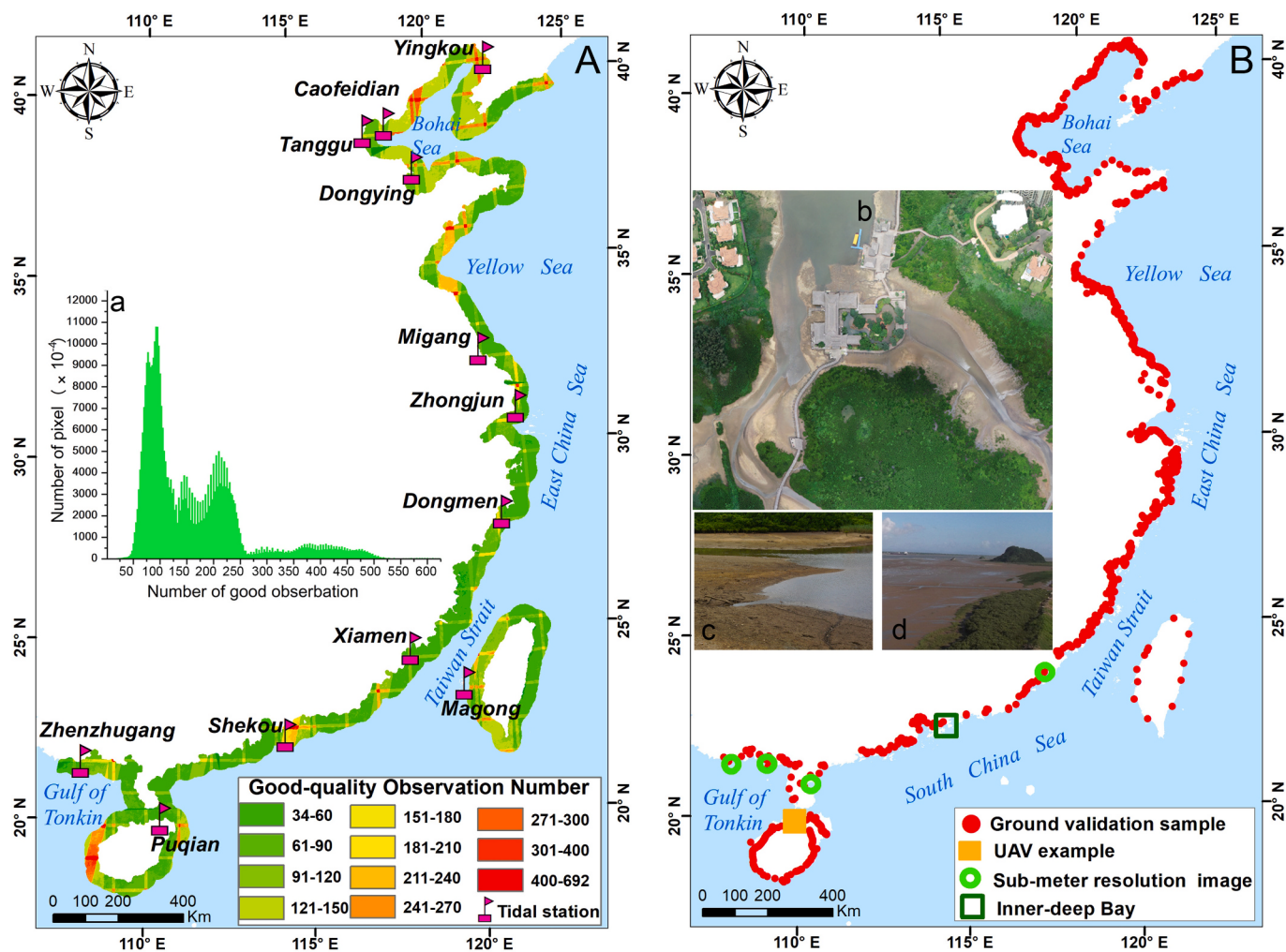


**Fig. 3.** Spatial distributions of Sentinel-2 good-quality observation number and key tide stations (A), and locations of ground validation samples (B). Insets: (a) Histogram of good observation numbers; (b) Unmanned aerial vehicle image of tidal flats in Fuliwan, Hainan Province, China, obtained during local lowest tide. (c) Ground photo of Fuliwan tidal flats. (d) Ground photo of tidal flats outside Zhenhaiwan Bridge, Guangdong.

**Table 1**  
Formulas of the spectral indices used in this study.

Name	Abbreviation	Equation
Nominalized Difference Vegetation Index	NDVI	$(\rho_{nir} - \rho_{red}) / (\rho_{nir} + \rho_{red})$
Enhanced Vegetation Index	EVI	$2.5 \times \frac{\rho_{nir} - \rho_{red}}{\rho_{nir} + 6\rho_{red} - 7.5\rho_{blue} + 1}$
Normalized Difference Water Index	NDWI	$\frac{(\rho_{green} - \rho_{nir})}{(\rho_{green} + \rho_{nir})}$
Modified Normalized Difference Water Index	mNDWI	$(\rho_{green} - \rho_{swir}) / (\rho_{green} + \rho_{swir})$
Normalized Difference Soil Index	NDSI	$(\rho_{swir} - \rho_{nir}) / (\rho_{swir} + \rho_{nir})$

Note:  $\rho_{nir}$  is the reflectance of the near-infrared band (Band 8, Central wavelength: 842 nm),  $\rho_{red}$  is the reflectance of the red band (Band 4, Central wavelength: 665 nm),  $\rho_{green}$  is the reflectance of the green band (Band 3, Central wavelength: 560 nm),  $\rho_{blue}$  is the reflectance of the blue band (Band 2, Central wavelength: 490 nm), and  $\rho_{swir}$  is the reflectance of a short-wave infrared band in Sentinel-2 images (Band 11, Central wavelength: 1610 nm).

Wang et al., 2020b). First, the coastal zone of China was partitioned into two classes of tidal flat and non-tidal flat only. The non-tidal flat category includes vegetation, built-up and permanent water. Second, we randomly selected the ground survey samples in each stratum using ArcGIS. At last, a total of 5479, 2617, 3828, and 3353 samples were selected as the ground validation samples for tidal flat, vegetation, built-

up land, and water categories, respectively. The ground validation samples we collected evenly distributed along the whole coasts of China (Fig. 3B).

#### 2.4.2. Identification of edge-points of fully exposed tidal flats

In this study, edge-points of fully exposed tidal flats were identified and collected as key references to validate the accuracy of the CTF map. To obtain the edge-points, firstly, we selected 12 key tide stations (Fig. 3A). From north to south, according to the length of coastlines in different climate zones, we selected 5 stations in the warm temperate, 5 stations in the subtropical, and 2 stations in the tropical zones. These stations are also located in different tide type coasts, i.e., 3 stations along the irregular diurnal tide zone, 3 stations along the regular diurnal tide zone, 3 stations along the irregular semi-diurnal tide zone, and 3 stations along the regular semi-diurnal tide zone. All these stations are adjacent to large patches of tidal flats. Tide tables of these stations were obtained from the website of China National Shipping Services (<https://www.cnss.com.cn/>). According to tide tables and transit time of Sentinel-2 satellites, 12 images that captured during the time of local lowest-tide were chosen to show fully exposed tidal flats. Information of those images and the instantaneous tide heights are summarized in Table 2. The lowest-tide Sentinel-2 image surrounding the Migang Tide Station, which is adjacent to the largest patch of tidal flats in China, illustrates the exposed tidal flat area that matched information from the intraday tide table (Fig. 4A). For each Sentinel-2 scene of the lowest-tide images,

**Table 2**

General characteristics of tide stations (from north to south), image acquisition time, and temporal tide status.

Province	Station name	Sentinel-2 transit time	Instantaneous tide height (cm)	Tide status
Liaoning	Yingkou	2019-05-02	-161	Local
		10:56:36		lowest
Heibei	Caofeidian	2019-09-02	-105	Local
		11:06:55		lowest
Tianjin	Tanggu	2019-09-02	-167	Local
		11:06:55		lowest
Shandong	Dongying	2019-07-21	-38	Local
		10:57:33		lowest
Jiangsu	Migang	2019-07-23	<b>-189</b>	<b>Local</b>
		10:48:48		lowest
Shanghai	Zhongjun	2019-03-15	-111	Local
		10:48:55		lowest
Zhejiang	Dongmen	2019-12-07	-128	Local
		10:39:46		lowest
Fujian	Xiamen	2019-09-21	-202	Local
		10:51:13		lowest
Taiwan	Magong	2019-01-26	-256	Local
		10:41:04		lowest
Guangdong	Shekou	2019-09-22	-68	Local
		11:11:30		lowest
Guangxi	Zhenzhugang	2019-04-15	-164	Local
		11:31:55		lowest
Hainan	Puqian	2019-06-07	-68	Local
		11:22:24		lowest

we randomly selected 50 pure tidal flat pixels and 50 pure non-tidal flat pixels along the edges of tidal flat patches as edge-points (Fig. 4B-D). In total, 1200 edge-points were collected. The pure tidal flat edge-points can reflect whether our resultant map contains fully exposed tidal flat patches. The pure non-tidal flat edge-points can be used to test whether high turbidity estuary water pixels are misclassified to tidal flats. Therefore, edge-points validation is a further verification for the accuracy of our resultant tidal flat map. Validation results derived from edge-points were lower than those derived from ground survey samples.

#### 2.4.3. Sub-meter resolution images of local lowest tide

Four sub-meter resolution satellite images, including two scenes of

Gaofen-2 imagery and two scenes of Google Earth imagery, captured during local lowest tide periods were collected to further validate our resultant map. The Google Earth imagery is made available by DigitalGlobe and CNES/Astrium (Liu et al. 2017). Locations of these images are shown in Fig. 3B with detailed information in Table 3.

#### 2.5. Methodologies for delineating tidal flat

##### 2.5.1. The maximum spectral index composite (MSIC) and Otsu algorithm (OA)

To catch fully exposed tidal flat, we developed a new mapping approach by integrating the maximum spectral index composite (MSIC) and Otsu algorithm (OA) and described it as the MSIC-OA approach. The MSIC, as we defined, sets each pixel in the composite based on which pixel in the time series Sentinel-2 image collection has the maximum value of a selected spectral index. In other words, in a composite image each pixel is selected from different image of time series Sentinel-2 image collection, and each pixel represents to the extreme tidal condition of its own position. To explain the MSIC, we provided a pseudocode (Table 4). In GEE platform the MSIC method could be executed using a function named “imageCollection.qualityMosaic()”, further explanations can be found at [https://developers.google.com/earth-engine/guides/ic\\_composite\\_mosaic](https://developers.google.com/earth-engine/guides/ic_composite_mosaic).

The OA could automatically find an optimal threshold that segment image into two classes based on the histogram of imagery (Otsu 1979).

**Table 3**

General characteristics of sub-meter imagery.

Location	Imagery	Resolution (m)	Acquisition time	Tide height (cm)	Tide status
Zhenzhu Harbor	Gaofen-2	0.8	2019-05-16 11:52:02	-123	Lowest
Beihai Bay	Gaofen-2	0.8	2019-05-26 11:55:54	-135	Lowest
Boti Harbor	Google Earth	0.28	2019-10-20 10:06:34	-105	Lowest
Zhangjiang Estuary	Google Earth	0.28	2019-10-03 10:00:05	-140	Lowest

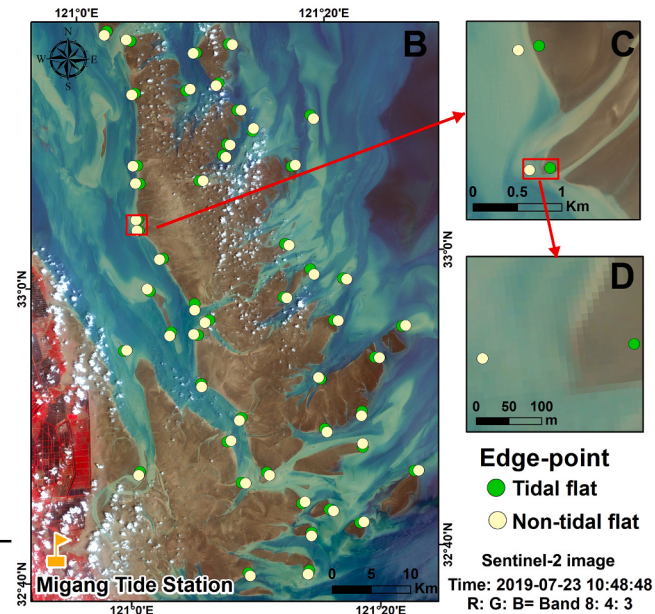
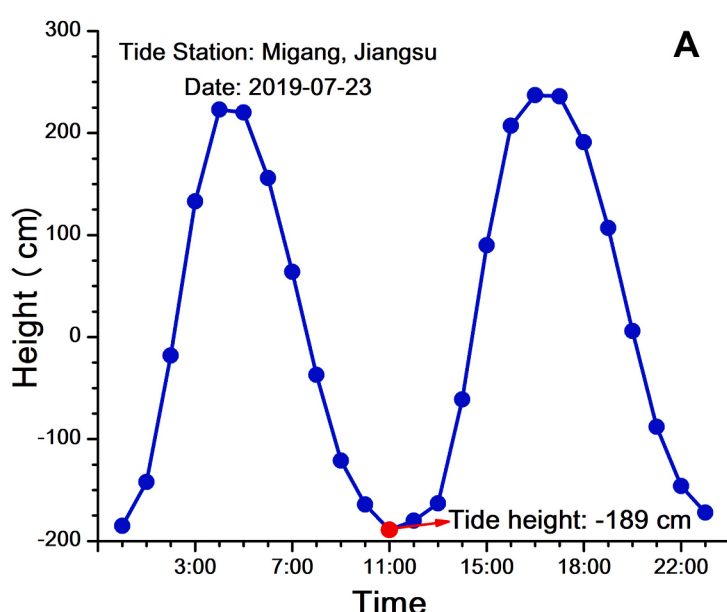


**Fig. 4.** Edge-points selection near the Migang Tide Station, Jiangsu, China. (A) Tide table of Migang Tide Station on 2019-07-23, the lowest tide occurred at 10:50:00 AM, with a tide height of -189 cm. (B) The Sentinel-2 image at the lowest-tide was captured at 10:48:48 AM. (B–D) Location of edge-points including 50 pure tidal flat points and 50 non-tidal flat points in this site.

**Table 4**

Process flow of the MSIC.

**Algorithm MSIC:** To make a composite which maximizes an arbitrary band in the input image collection

**Input:** an image collection  $imgCol$ , each image  $img_i$  in the  $imgCol$  has some bands; A band name  $strBand$ , the specified band based on whose values to composite.

**Output:** an image  $img$  which has a maximum value for the  $strBand$  composed from  $imgCol$ .

- 1: obtaining all the pixel locations  $LocMatrix$  of the  $imgCol$ ;
- 2: at each pixel location  $PixLocation_{i,j}$  in the  $LocMatrix$ , comparing the values for  $strBand$  in each image  $img_i$  in the  $imgCol$ , pick up the pixel  $Pixel_{i,j}$  with maximal value for  $strBand$ ;
- 3: compositing all the pixels  $Pixel_{i,j}$  to an image  $img$ ;
- 4: return  $img$ .

This technique was recently used to build a GEE-based tool for assessing the change in surface water at the global scale (Donchyts et al. 2016), and also achieved satisfying results in other studies (e.g., Gong et al. 2020; Zhao et al. 2020b). In the OA, the optimal threshold is found based on maximizing inter-class variance (equivalently, minimizes the sum of intra-class variances) as Eq. (1).

$$BSS = \sum_{k=1}^p (\bar{V}_k - \bar{V})^2 \quad (1)$$

where BSS represents between-sum-of-squares, describing the variance structure of a dataset,  $p$  is the number of classes, in this study  $p = 2$ .  $V$  is the value of the band that was selected to divide different classes. Class  $k$  is defined by every  $V$  less than a certain threshold; thus, the optimal threshold is that maximizes the BSS.

### 2.5.2. Compositing the maximal and minimal water extent images

There are mainly three types of land cover adjacent to tidal flats, i.e. water, vegetation, and built-up land (e.g., dam, port, and outer edge of pond). To analyze the spectral characteristics of different land covers, we randomly selected 200 ground survey samples for each land cover type and overlaid these samples to local lowest tide images. The surface reflectance and spectral indices of fully exposed tidal flat, vegetation, water, and built-up land are shown in Fig. 5A and B.

To synthesize a maximal water extent image, we need to generate a MSIC image with a spectral index which is sensitive to water. According to Fig. 5B, both NDWI and mNDWI can meet this requirement. However, previous studies indicate that NDWI is less sensitive to water that contains vegetation or surrounded by built-up land (Singh et al. 2015; Xu

2006). In contrast, Singh et al. (2015) and Wicaksono and Wicaksono (2019) concluded that mNDWI performed better than NDWI for extracting water covered by vegetation (Singh et al. 2015; Wicaksono and Wicaksono, 2019). Whereas, other studies claimed that non-water areas, for example, moist soil, could be included in mNDWI derived water extraction results (Yang et al. 2015).

In this study, we produced two MSIC images based on NDWI and mNDWI, namely NDWI-MSIC and mNDWI-MSIC, respectively. NDWI and mNDWI distributions in the NDWI-MSIC and mNDWI-MSIC images are shown in Fig. 6A and B, respectively. According to our field surveys and previous literatures, the maximal water extent should include areal extents of both permanent water and tidal flats (Zhang et al. 2019). However, as shown in Fig. 6A, the NDWI-MSIC only highlighted permanent water. In contrast, the mNDWI-MSIC highlighted both permanent water and tidal flats (Fig. 6B). Therefore, the mNDWI-MSIC is optimal to catch the highest waterline and represent the maximal water extent. As shown in Fig. 6B, mNDWI-MSIC suppressed the built-up land effectively, so that artificial shorelines, such as dams, roads, and outer edges of ponds could be effectively distinguished. This characteristic supports particularly to intertidal and inland regions (Xu and Gong 2018). Therefore, mNDWI-MSIC was adopted to reflect the maximal water extent in this study.

To obtain the minimal water extent, i.e., the lowest tide condition, it is essential to find an index that has higher values of non-water (vegetation and tidal flat) than water pixels. As shown in Fig. 5B, both NDVI and EVI can meet this requirement. While NDSI was designed to identify soil in coastal marsh (Rogers and Kearney 2003), it could not distinguish tidal flat from water. In the NDSI image, water and tidal flat has similar NDSI values (Fig. 5B), because, as shown in Fig. 5A, the trends in reflectivity of tidal flat and water are similar in short-wave infrared and near infrared bands (NDSI was built based on these two bands, Table 1). Therefore, we produced two MSIC images based on NDVI and EVI, namely NDVI-MSIC (Fig. 6C) and EVI-MSIC (Fig. 6D), respectively. We found a few water pixels mixed with tidal flat and built-up land. This is because EVI is derived using blue band which is sensitive to coastal turbid water (Hu et al. 2000). In contrast, the NDVI-MSIC could separate tidal flat from water robustly (Fig. 6C). Therefore, the NDVI-MSIC was chosen to reflect the minimal water extent.

### 2.5.3. Automatically delineate tidal flats from the MSIC images

In this study, the OA was applied to mNDWI-MSIC image to create a binary classification result that reflected the maximal water extent. It is

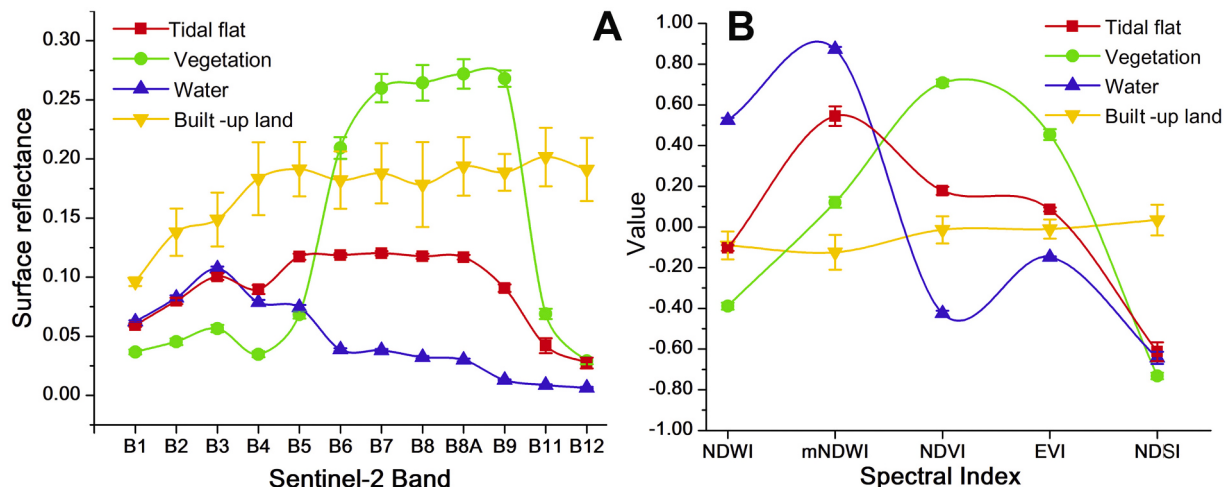


**Fig. 5.** The surface reflectance and spectral index values of different land cover types (statistics based on ground survey samples). (A) Surface reflectance profiles of each land cover types with standard deviation. (B) Values of spectral indices of each land cover types with standard deviation. We randomly selected 200 ground survey samples for each land cover type and overlaid the samples to local low tide images. Tidal flat here refers to fully exposed tidal flat pixel, water here refers to both seawater and inland water, vegetation here refers to intertidal vegetation and inland vegetation.

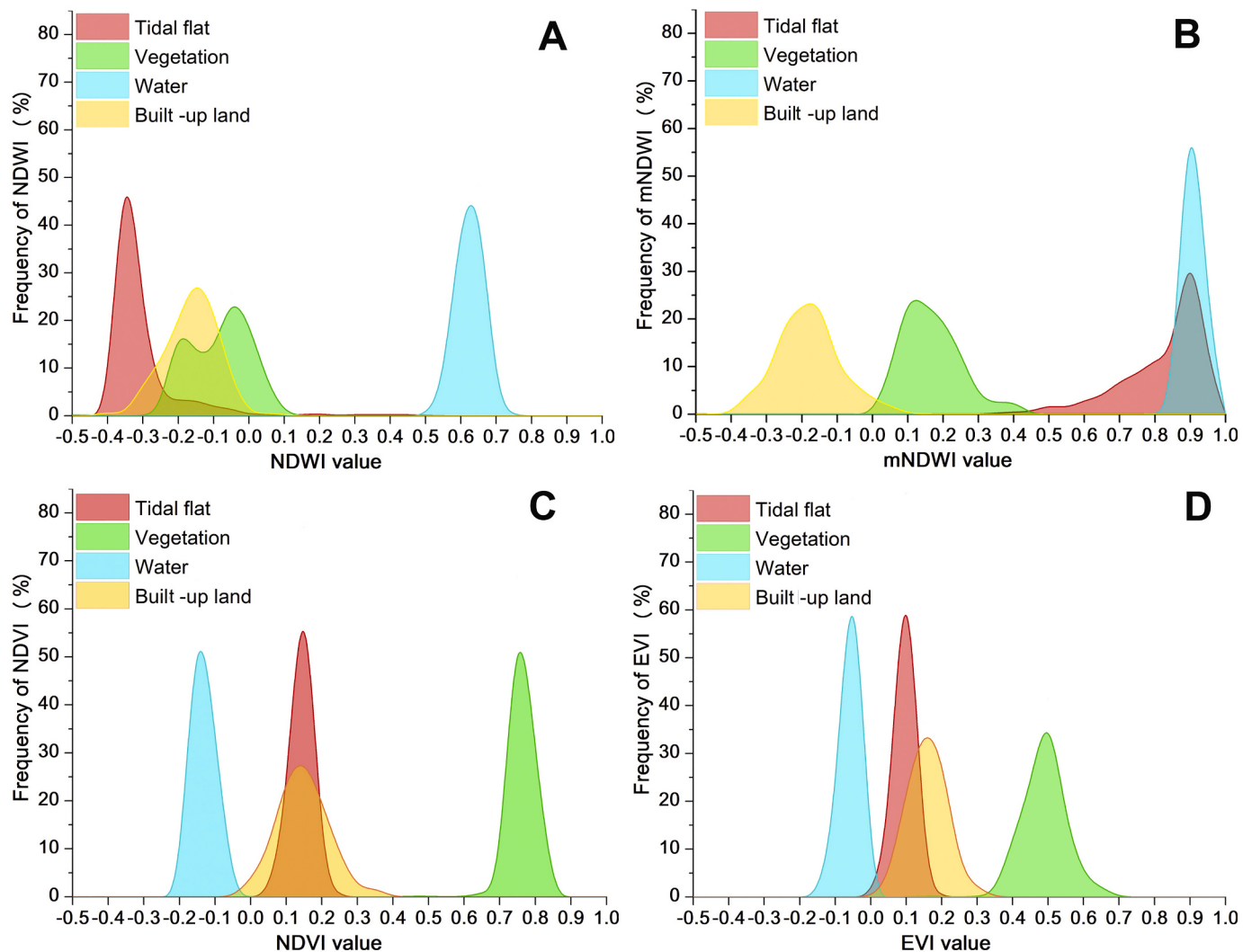


**Fig. 6.** Histograms of different land covers in different MSIC images. (A) Histograms of different land covers in the NDWI-MSIC image. (B) Histograms of different land covers in the mNDWI-MSIC image. (C) Histograms of different land covers in the NDVI-MSIC image. (D) Histograms of different land covers in the EVI-MSIC image. Tidal flat here refers to fully exposed tidal flat, water here refers to permanent water.

notable that the original maximal water extent directly obtained from OA contained inland water surfaces such as aquaculture ponds, lakes, and reservoirs. As mNDWI efficiently depressed built-up lands around these water surfaces, inland water surfaces were not directly connected to seawater. Therefore, we could automatically reserve the largest patch of water as the maximal water extent.

In the NDVI-MSIC image, the NDVI value of coastal vegetation is much higher than that of water and tidal flat (Fig. 6C). In this case, applying the OA directly to the NDVI-MSIC image could produce a binary classification of vegetation and non-vegetation. To address this problem, first, we applied OA to NDVI-MSIC to get the intertidal vegetation extent; and then, erased the vegetation extent form the NDVI-MSIC to get an image that contains water and tidal flat only (image of water and tidal flat); At last, we applied OA to the image of water and tidal flat and obtained the extents of tidal flats.

#### 2.5.4. A case study

To further explain how MSIC-OA approach works, we chose Inner-deep Bay (Location is shown in Fig. 3B) as a case study area. The workflow is described as below.

- (1) Selecting mNDWI as the spectral index to composite the maximal water extent image (mNDWI-MSIC), shown as Fig. 2a. Each pixel

in Fig. 2a has the maximum mNDWI value of times series pixels of its own position.

- (2) Selecting NDVI as the spectral index to composite the minimal water extent image, shown as Fig. 2b. Each pixel in Fig. 2b has the maximum NDVI value of times series pixels of its own position.
- (3) Applying Otsu algorithm to mNDWI-MSIC to get the maximal water extent (Fig. 2c), and using the maximal water extent to clip the minimal water image (Fig. 2b). Thus, we create an image of intertidal area which contains seawater, tidal flat, and intertidal vegetation (Fig. 2d).
- (4) Applying Otsu algorithm to Fig. 2d to get the maximal intertidal vegetation extent, and erasing the maximal intertidal vegetation extent from Fig. 2d. Thus, we created an image that contained only seawater and tidal flat (Fig. 2e).
- (5) At last, applying Otsu algorithm to Fig. 2e, and finally tidal flats were delineated (Fig. 2f).

#### 2.6. Validation of the CTF map

Validation of the CTF map includes three aspects: first, point-to-point validation using a confusion matrix derived from ground survey samples; second, confusion matrix derived from tidal flat edge-points; and third, polygon-to-image comparison based on sub-meter resolution

images.

For the first and second aspects, we produced confusion matrices and calculate overall accuracy and F1 score of tidal flat category. Overall accuracy represents to the proportion of ground survey samples mapped correctly. F1 score is a harmonic mean of producer's accuracy and user's accuracy, which indicates the classification capability of a single class (Zhong et al. 2019).

For the polygon-to-image comparisons, we overlaid our resultant tidal flat map on four sub-meter resolution images (locations are shown in Fig. 3B). The comparisons were aimed to confirm the consistency of edges and shapes between our resultant map and sub-meter resolution images.

## 2.7. Other tidal flat maps of China

Murray et al. (2019) at the University of Queensland produced a global tidal flat dataset (UQD from 1984 to 2016 (available at <https://www.intertidal.app/download>). Tidal flat maps in this dataset were produced in GEE platform based on all available Landsat imagery, random forest algorithm, and 10,701 geo-referenced training points. The definition of tidal flats in UQD dataset was as same as this study, so we chose their latest tidal flat map (map of 2016) to compare with our resultant map.

Wang et al., 2020a at the Fudan University and University of Oklahoma used the GEE platform and a decision tree algorithm to generate annual maps of coastal tidal flats in China during 1986–2016 at 30-m spatial resolution. Additionally, Wang et al., 2020b updated their tidal flat maps to a more detailed coastal wetland map (tidal flat, evergreen wetland, and deciduous wetland) for 2018. The updated map (FUDAN/OU) was generated by a new pixel- and phenology-based algorithm and time series Landsat imagery in GEE. The definition of intertidal flats in the FUDAN/OU map was also as same as ours, so the updated FUDAN/OU map was also chosen to be compared with our resultant map.

In addition to the national scale tidal flat datasets, there were several studies focusing on mapping tidal flats at regional scale of China. Recently, Zhao et al. (2020b) at the Institute of Geographical Sciences and Natural Resources Research utilized Sentinel-1 Synthetic Aperture Radar data during 2014–2018 to generate a 10-m spatial resolution map of tidal flat in southern China (IGSNRR). The tidal flat they defined was area being water during high tides and being land during low tides, which is similar as ours. For this reason, IGSNRR map was also selected to compare with our resultant map.

## 3. Results

### 3.1. Accuracy assessments of the CTF map

The national and provincial point-to-point validations based on the ground validation samples are shown in Table 5. The overall accuracy of the CTF map is 0.94, and tidal flat category had a F1 score of 0.93. In provincial level, Hebei and Guangxi had the highest overall accuracy of 0.97, and Shanghai had the lowest overall accuracy of 0.89. Likewise, Hebei and Guangxi had the highest F1 score of 0.95, and Shanghai had the lowest F1 score of 0.85. The confusion matrix demonstrated that the CTF map is highly consistent with ground validation samples.

Point-to-point validation of the CTF map based on the edge-points is shown in Table 6. The F1 score and overall accuracy is 0.94 and 0.94, respectively. The producer's accuracy and user's accuracy of tidal flat category is 0.90 and 0.98, respectively. The edge-points based validation confirmed that the edges of tidal flat patches in the CTF map is highly consistent with ground measurements.

To further evaluate the accuracy, we overlaid the CTF map on four sub-meter resolution lowest tide images (Table 3). As illustrated in Fig. 7, the shapes and edges of derived CTF patches are highly consistent with the sub-meter resolution lowest-tide images. Noticeably, small patches of deciduous salt marshes (*Spartina alterniflora*, an invasive

**Table 5**

Confusion matrix of tidal flats (TF) validation based on ground validation samples.

Region	Class	TF	Non-TF	Use. acc.	F1 score	Ove. acc.
China	TF	5006	473	0.91	0.93	0.95
	Non-TF	316	9482	0.97	0.96	
	Pro. acc.	0.93	0.95			
Liaoning	TF	357	30	0.92	0.93	0.95
	Non-TF	20	643	0.97	0.96	
	Pro. acc.	0.95	0.96			
Hebei	TF	257	15	0.94	0.95	0.97
	Non-TF	13	621	0.98	0.98	
	Pro. acc.	0.95	0.98			
Tianjin	TF	298	22	0.93	0.94	0.96
	Non-TF	14	594	0.98	0.97	
	Pro. acc.	0.96	0.96			
Shandong	TF	498	52	0.91	0.92	0.94
	Non-TF	35	879	0.96	0.95	
	Pro. acc.	0.93	0.94			
Jiangsu	TF	685	86	0.89	0.91	0.95
	Non-TF	42	1567	0.97	0.96	
	Pro. acc.	0.94	0.95			
Shanghai	TF	244	48	0.84	0.85	0.89
	Non-TF	36	463	0.93	0.92	
	Pro. acc.	0.87	0.91			
Zhejiang	TF	396	60	0.87	0.89	0.92
	Non-TF	36	734	0.95	0.94	
	Pro. acc.	0.92	0.92			
Fujian	TF	311	32	0.91	0.93	0.96
	Non-TF	13	657	0.98	0.97	
	Pro. acc.	0.96	0.95			
Taiwan	TF	289	16	0.95	0.94	0.96
	Non-TF	21	597	0.97	0.97	
	Pro. acc.	0.93	0.97			
Guangdong	TF	671	39	0.95	0.94	0.96
	Non-TF	42	1345	0.97	0.97	
	Pro. acc.	0.94	0.97			
Guangxi	TF	567	32	0.95	0.95	0.97
	Non-TF	24	1047	0.98	0.97	
	Pro. acc.	0.96	0.97			
Hainan	TF	433	41	0.91	0.93	0.96
	Non-TF	20	956	0.98	0.97	
	Pro. acc.	0.96	0.96			

Note: The ground survey samples in Guangdong Province including those of Hong Kong and Macao. Use. means User's, Pro. means Producer's, Ove. means Overall, acc. Means accuracy.

**Table 6**

Confusion matrix of tidal flats (TF) validation based on the edge-points.

Class	TF	Non-TF	Total	Use. acc.	F1 score	Ove. acc.
TF	542	10	552	0.98	0.94	0.94
Non-TF	58	590	648	0.91	0.95	
Total	600	600	1200			
Pro. acc.	0.90	0.98				

Note: Use. means User's, Pro. means Producer's, Ove. means Overall, acc. Means accuracy.

exotic species) in the Zhangjiang Estuary (Fig. 7D) were precisely extracted and separated from the tidal flats.

### 3.2. Geographical characteristics of the CTF map

Fig. 8 illustrates the spatial distribution of tidal flats presented in the CTF map along the entire coastal line of China and examples of seven sub-regions. The national, provincial areal extents of tidal flat, and mean tidal flat width, i.e., tidal flat area divided by coastline length, of each province are shown in Table 7. The total area of tidal flats in China was mapped as 858,784 ha. Jiangsu Province accounted for the largest proportion (24%), followed by Zhejiang, Fujian, Shandong, and Liaoning Provinces. Those five provinces held about 73% of the total tidal flats in China.

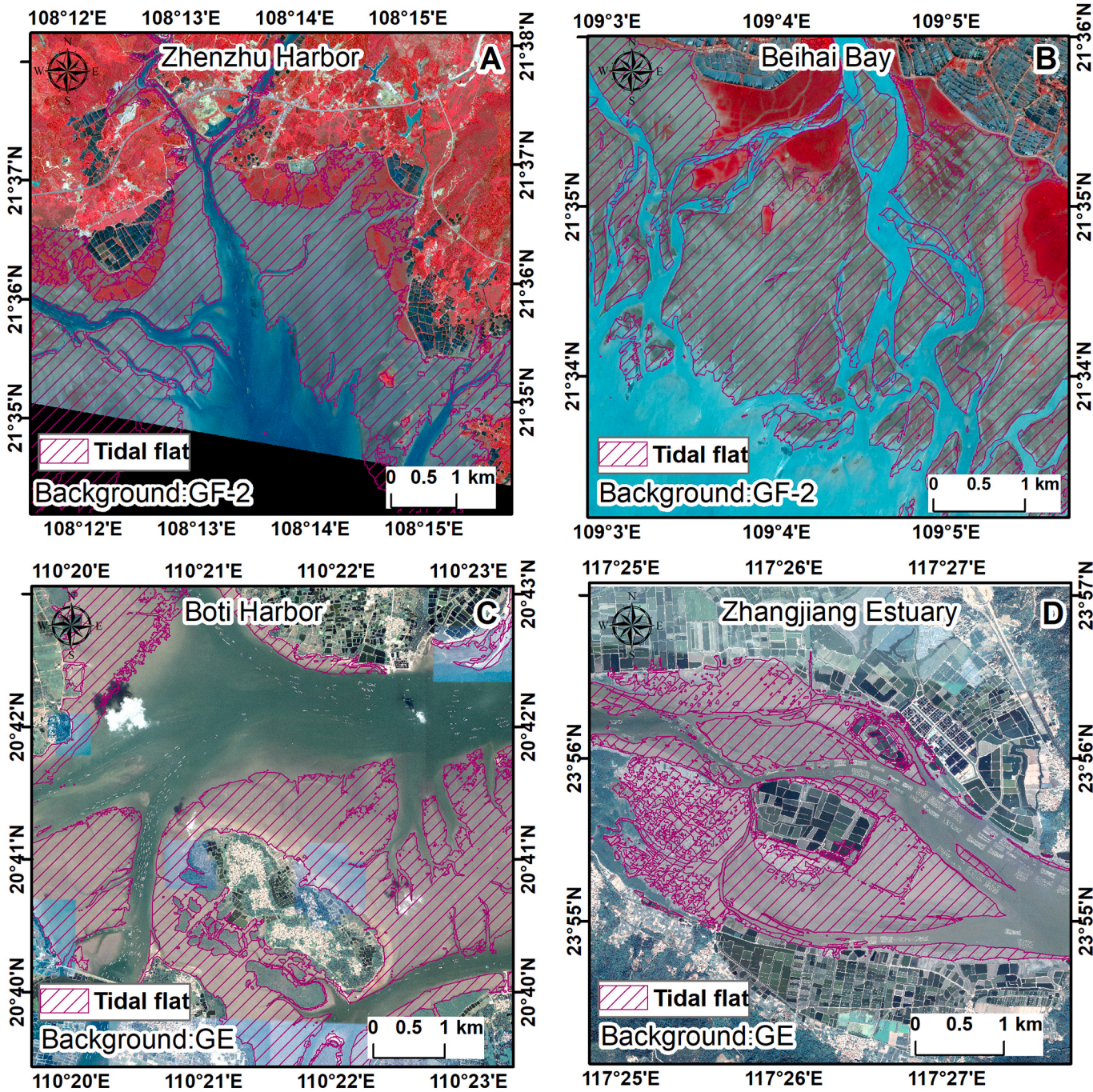


**Fig. 7.** Regional subsets of the CTF map overlaid on sub-meter resolution lowest tide images. Subset of the CTF map overlaid on Gaofen-2 image in (A) Zhenzhu Harbor, Guangxi, (B) Beihai Bay, Guangxi. Subsets of the CTF along with GE image in (C) Boti Harbor, Guangdong, and (D) Zhanjiang Estuary, Fujian.

**Fig. 8a-g** illustrate tidal flats in the six largest estuaries of China. As we mapped, from north to south, the estuaries of the Liao (**Fig. 8a**), Hai (**Fig. 8b**), Yellow (**Fig. 8c**), Yangtze (**Fig. 8e**), Min (**Fig. 8f**), and Pearl rivers (**Fig. 8g**) had tidal flats of 38,168 ha, 12,643 ha, 38,782 ha, 53,501 ha, 5525 ha, and 7729 ha, respectively, accounted for 18% of the total. Along the coasts of China, ten tidal flat patches contained with an area larger than 10,000 ha. The top four largest patches were all found along the southern Jiangsu coasts (**Fig. 8d**), with an area of 50,111 ha, 35,020 ha, 33,628 ha, and 26,563 ha, respectively. In terms of distribution along different tide types, regular semi-diurnal tide regions had the largest area of tidal flats (503,373 ha), followed by irregular semi-diurnal tide regions (246,257 ha), regular diurnal tide regions

(58,414 ha), and irregular diurnal tide regions (50,751 ha).

#### 4. Discussion

##### 4.1. Reliability of our tidal flat mapping

This study developed a MSIC-OA approach for mapping China's tidal flats through time series Sentinel-2 imagery on the GEE platform. It is the first investigation to map tidal flats at a 10-m spatial resolution along the entire coastline of China. The successful implementation of this study was attributed to three factors, i.e., improved capacity of satellite data by Sentinel-2 imagery, the robust MSIC-OA approach, and the

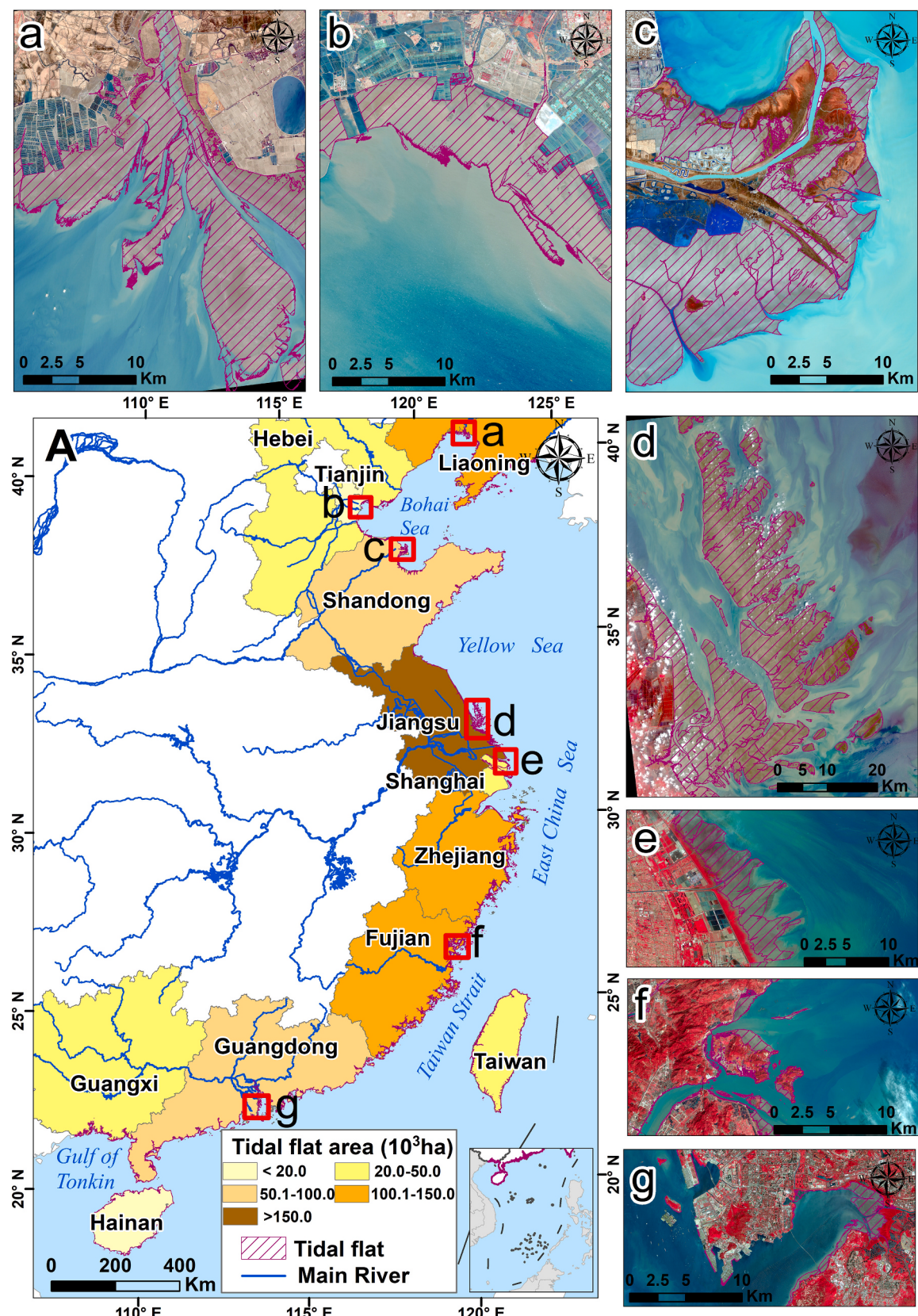


**Fig. 8.** Distribution and areal extent of tidal flats along the coasts of China (A). (a) Tidal flats in the Liao River Estuary, (b) tidal flats in the Hai River Estuary, (c) tidal flats in the Yellow River Estuary, (d) the top four largest tidal flat patches, (e) tidal flats in the Yangtze River Estuary, (f) tidal flats in the Min River Estuary, and (g) tidal flats in the Pearl River Estuary. (For interpretation of the references to colour in this figure legend, the reader is referred to the web version of this article.)

**Table 7**

National and provincial areas, percentages, and mean widths of tidal flat.

Province	Tidal flat area ( $10^4 \text{ m}^2$ )	Percentage (%)	Coastline length ( $10^3 \text{ m}$ )	Mean tidal flat width (m)
Liaoning	101,114	11.77	2803	361
Hebei	35,021	4.08	391	890
Tianjin	10,474	1.22	798	135
Shandong	104,612	12.18	3479	286
Jiangsu	204,135	23.77	1302	1577
Shanghai	35,590	4.14	302	1140
Zhejiang	113,192	13.18	2173	521
Fujian	106,670	12.42	2976	358
Taiwan	22,577	2.63	4056	56
Guangdong	62,078	7.23	1173	529
Guangxi	46,935	5.47	1912	245
Hainan	16,381	1.91	1589	103
Total	858,784	100.00	22,954	374

Note: The tidal flats in Guangdong province including those of Hong Kong and Macao. The lengths of coastline were acquired from [Hou et al. \(2016\)](#).

immense computing power of the GEE platform. The extensive ground-based validation efforts confirmed the value of this approach.

Firstly, the open-accessed Sentinel-2 imagery enhanced the capability of monitoring the constantly changing intertidal environments, due to its high temporal frequency (2–5 days' revisit circle) and finer spatial resolution (10-m; [Jia et al., 2019](#)). Frequency of observation is fundamental to develop a reliable tidal flat map, because such mapping efforts are based on the assumption of availability of images acquired at the time close to the lowest and highest tides. Compared to Landsat series, Sentinel-2 series improved the frequency of observation by more than three times, from 10 to 50 ([Wang et al., 2020b](#)) to 40–210 revisits over the entire coasts of China for the mapped period. In addition, tidal flat is a narrow and patchy landscape feature ([Cao et al. 2020](#)). The finer spatial resolution of Sentinel-2 imagery offers great opportunities to obtain maps with more spatial details.

Secondly, instead of selecting the highest and lowest tide images from 28,367 scenes, we adopted the MSIC approach, which can synthesize the highest and lowest tide images rapidly and robustly. The innovative MSIC-OA combination has three unique advantages. First, the MSIC-OA is a full-automatic approach, which does not require manual intervention, or training samples, or auxiliary information in the mapping process. Second, no additional masking or pre- and post-processing steps are necessary to revise the original mapping results. In the MSIC-OA approach, the maximal water extent only contains marine environments, because the mNDWI-MSIC image effectively suppress the artificial shoreline and other impervious surface. Third, the MSIC overcomes the uncertainties derived from tidal variations within a scene. Pixel-based image compositing could overcome this difficulty. Each pixel in the composite image is selected based on which pixel in the time series image collection has the maximum value of a selected spectral index, such as mNDWI and NDVI as employed in this study. In other words, in the composite image each pixel is selected from different scene, and each pixel represents an extreme tidal condition, i.e. the lowest or highest tide of its own position.

Thirdly, the GEE enabled quick access and process a massive number of Sentinel-2 images in a paralleled process ([Dong et al. 2016](#); [Tian et al. 2020](#)). Specifically, the GEE synchronizes all the Sentinels' data and provides different levels of processed products, including the top of atmosphere and surface reflectance data.

#### 4.2. Uncertainties in tidal flat mapping

The uncertainties of the CTF map were mainly caused by four factors. First, even though over 75% of the pixels have more than 60 good-quality observations, it is almost impossible to capture images at the absolute lowest and highest tides for all locations along the 22,954 km coastline of China. Thus, we searched tide tables of the key tide stations

([Fig. 3A](#) and [Table 3](#)) according to the transit time of Sentinel-2A/B satellites, and found that (1) there were 18–24 and 6–11 opportunities of obtaining the lowest tide images in semi-diurnal and diurnal tide coasts, respectively; (2) there were 16–23 and 7–10 opportunities of obtaining the high tide images in semi-diurnal and diurnal tide coasts, respectively; As shown in [Fig. 1](#), over three fourth of China's coasts are affected by semi-diurnal tides, which means tidal flats along these coasts have higher probability to be precisely mapped than those along diurnal tides coasts.

Second, although this study removed clouds based on QA60 band, a few small regions were still covered yet by clouds that affected tidal flats identification. Third, high turbidity estuary water may not be completely separated from tidal flats. This could explain, for example, why Shanghai at the estuary of the Yangtze River had the lowest mapping accuracy. Fourth, small patches of seaward reclamation areas may be classified to tidal flats. Although most of the coastal reclamation areas were protected by artificial seawalls in China, there were still small patches of offshore ponds or ports. For example, offshore ponds in Tongming Sea, Guangdong Province would be submerged by high tide and could be misclassified as tidal flats.

#### 4.3. Comparisons with other tidal flat maps

The comparisons between the CTF map and other tidal flat maps showed the difference of areal extents ([Fig. 9](#)). In summary, the CTF map had a much smaller tidal flat area than the UQD map, and a larger area than the FUDAN/OU and the IGSNRR maps. [Fig. 10](#) illustrates the comparisons of subsets in Liao Estuary, Liaoning (zone A), Lian Estuary, Guangxi (zone B), and Jiulong Estuary, Fujian (zone C).

The differences between the CTF and UQD maps can be mostly attributed to the mapping methods. The UQD dataset was derived based on random forest algorithm and a huge number of training samples, although the authors built a coastal data-mask, large extents of inland bare lands, aquaculture ponds, and intertidal salt marshes were included into tidal flats ([Fig. 10A\\_UQD](#), [B\\_UQD](#), and [C\\_UQD](#)).

[Fig. 9](#) shows that the CTF map had a larger areal extent of tidal flat than the FUDAN/OU in every province. The differences can be attributed to the data sources, i.e., Landsat vs. Sentinel-2. Due to the patchy and narrow pattern of tidal flat, Sentinel-2 images with a 10-m spatial resolution are capable of detecting more tidal flat areas ([Fig. 10A\\_CTF](#), [B\\_CTF](#), and [C\\_CTF](#)) than Landsat images with a 30-m resolution ([Fig. 10A\\_FUDAN/OU](#), [B\\_FUDAN/OU](#), and [C\\_FUDAN/OU](#)). More importantly, due to the variability of tide, Sentinel-2 with a 2–5 days revisit circle has expended frequency and more opportunities to capture fully exposed tidal flats than Landsat's 8–16 days by Landsat 7 and

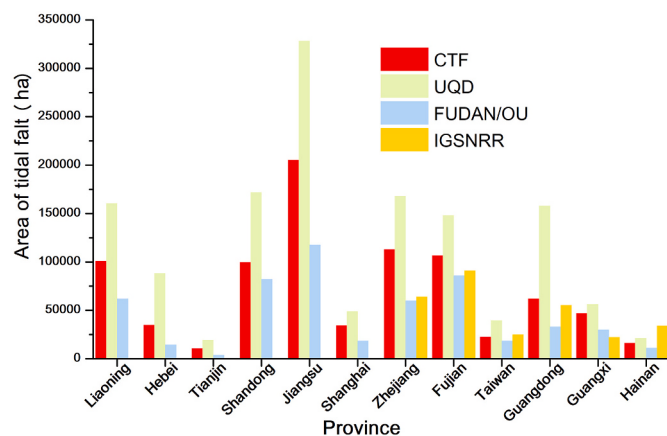


**Fig. 9.** Provincial comparisons between China\_Tidal Flat (CTF) map and other maps, including UQD ([Murray et al. 2019](#)), FUDAN/OU ([Wang et al., 2020b](#)), and IGSNRR ([Zhao et al. 2020b](#)).

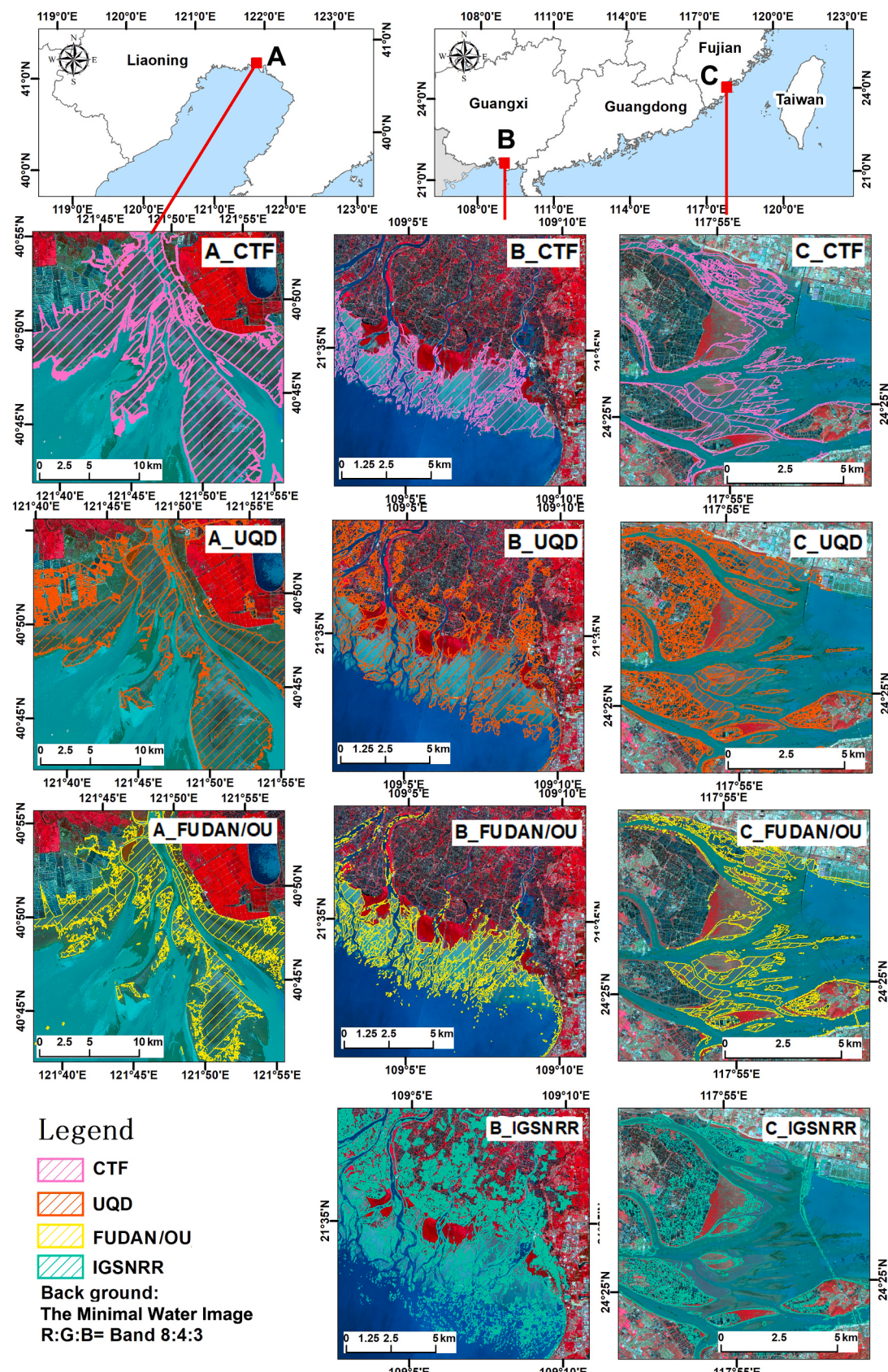


**Fig. 10.** Subset views of tidal flats from the CTF map, the UQD map (Murray et al. 2019), the FUDAN/OU map (Wang et al., 2020b), and the IGSNRR map (Zhao et al. 2020b) in the Liao Estuary, Liaoning (zone A), Lian Estuary, Guangxi (zone B), and Jiulong Estuary, Fujian (zone C).

## Landsat 8.

The differences between the CTF and IGSNRR maps can be attributed to the different method in building the lowest and highest tide images. The IGSNRR map used a quantile synthesis method, which assumed a low (5%) and high (95%) quantile to be the lowest and highest tidal data, respectively. However, since the lowest and highest tides appear only in a short time period, there is a high probability that the lowest and highest tides contained in the lower than 5% and higher than 95% quantile, respectively. In contrast, the CTF map built the lowest and the highest tide images based on MSICs, which composited all the pixels that ever covered by water as the maximal water extent image in the highest tides, and pixels ever exposed as the minimal water extent image in the lowest tides. Therefore, the tidal flat areas of the CTF map is larger than the IGSNRR's. Also the IGSNRR had misclassified inland reservoirs and ponds into tidal flat category (Fig. 10B\_IGSNRR, and C\_IGSNRR).

## 4.4. Potential applications of the CTF map and the MSIC-OA approach

The CTF map provides up-to-date information on tidal flats distribution at a 10-m spatial resolution along the entire coastline of China. This map can be used to support a broad scope of coastal management and policymaking related to sustainable use of tidal flats (Bell et al. 2016). For example, aligning with the SDG 14, China's State Council announced to enhance coastal protection and control reclamation activities since 2018. The CTF map with updated and detailed spatial information is essential for decision making in selection of coastal development districts. The CTF map can facilitate the efforts of managing relevant coastal ecosystems, such as mangrove afforestation (Jia et al. 2018) and control of *Spartina alterniflora* invasion (Mao et al. 2019). The CTF map can be used as baseline data for scientific researches, such as biodiversity conservation and migratory bird protection, carbon storage estimation, sea-level rise impaction, and coastal erosion (Brockmann and Stelzer 2008; Jorgenson and Brown 2005; Sagar et al. 2017).

In this study, the MSIC-OA approach, time series Sentinel-2 images, and the GEE platform are proved to be effective in rapid, robust, and automated mapping of tidal flats. The MSIC-OA approach has great potential to be applied in detection of land cover dynamics, such as phenological processes in monitoring of croplands, forests, grasslands, and wetlands. However, because the Sentinel-2A satellite was initially launched in 2015, it could not provide extensive historical observations. To track long-term dynamics of tidal flats, integration of other satellite data, for example, the Landsat imagery is needed. In addition, to overcome the errors caused by the limitation of cloud-free observations, microwave images from Sentinel-1 can be combined with optical images.

## 5. Conclusions

Due to the nature of tidal variation, mapping patchy features of tidal flats over extensive areas has been recognized as a great challenge. Previous efforts in mapping tidal flats relied on either auxiliary data or manual intervened pre-and post-processing. Meanwhile, the existing national-scale tidal flat maps of China were commonly derived from Landsat imagery with limitations of spatial and temporal resolutions.

To address these issues, we developed a rapid, robust, and automated approach, named MSIC-OA approach, to map tidal flats from time series Sentinel-2 imagery. The basic consideration of the MSIC-OA approach is to composite images with the maximal and minimal water extent coverages, and then, use the OA to automatically extract tidal flat areas and distributions. With the complete storage of Sentinel-2 images and computing power of GEE platform, the MSIC-OA approach succeeded in mapping tidal flats over the entire coastline of China.

This study produced the first 10-m spatial resolution tidal flat map of China, i.e., the CTF map. The finer spatial resolution identified more spatial details of tidal flats than those Landsat-based datasets (30-m).

The short revisiting cycle (2–5 days) of Sentinel-2 satellites greatly improved the opportunities of catching the fully exposed tidal flats. According to the point-to-point (including ground samples and edge-points) and polygon-to-image accuracy assessments, the CTF map achieved high overall accuracies and F1 scores, and highly consistent with sub-meter resolution images. Therefore, the CTF map can provide reliable information for the efforts of tidal flats management, sustainable development of coastal zones, and other related SDGs and scientific researches.

## Declaration of Competing Interest

The authors declare that they have no known competing financial interests or personal relationships that could have appeared to influence the work reported in this paper.

## Acknowledgments

This work is jointly supported by the Strategic Priority Research Program of the Chinese Academy of Sciences (XDA19040500), the National Natural Science Foundation of China (4173064, 41671219, 41771383, and U1901215), the Youth Innovation Promotion Association of Chinese Academy of Sciences, the Open Fund of State Laboratory of Information Engineering in Surveying, Mapping and Remote Sensing, Wuhan University (Grant No. 19I02), the Science and Technology Development Program of Jilin Province (No. 20200301014RQ), and the National Earth System Science Data Center ([www.geodata.cn](http://www.geodata.cn)).

## Appendix A. Supplementary data

Supplementary data to this article can be found online at <https://doi.org/10.1016/j.rse.2021.112285>.

## References

- Barbier, E.B., Koch, E.W., Silliman, B.R., Hacker, S.D., Wolanski, E., Primavera, J., Graneck, E.F., Polasky, S., Aswani, S., Cramer, L.A., 2008. Coastal ecosystem-based management with nonlinear ecological functions and values. *Science* 319, 321–323.
- Bell, P.S., Bird, C.O., Plater, A.J., 2016. A temporal waterline approach to mapping intertidal areas using X-band marine radar. *Coast. Eng.* 107, 84–101.
- Brockmann, C., Stelzer, K., 2008. Optical remote sensing of intertidal flats. In: Barale, V., Gade, M. (Eds.), *Remote Sensing of the European Seas*. Springer, Netherlands, pp. 117–128.
- Campbell, A., Wang, Y., 2018. Examining the influence of tidal stage on salt marsh mapping using high-spatial-resolution satellite remote sensing and topobathymetric lidar. *IEEE Trans. Geosci. Remote Sens.* 56, 5169–5176.
- Campbell, A., Wang, Y., 2019. High spatial resolution remote sensing for salt marsh mapping and change analysis at Fire Island National Seashore. *Remote Sens.* 11, 1107.
- Campbell, A.D., Wang, Y., 2020. Salt marsh monitoring along the mid-Atlantic coast by Google Earth engine enabled time series. *PLoS One* 15, e0229605.
- Cao, W., Zhou, Y., Li, R., Li, X., 2020. Mapping changes in coastlines and tidal flats in developing islands using the full time series of Landsat images. *Remote Sens. Environ.* 239, 111665.
- Chen, B., Xiao, X., Li, X., Pan, L., Doughty, R., Ma, J., Dong, J., Qin, Y., Zhao, B., Wu, Z., Sun, R., Lan, G., Xie, G., Clinton, N., Giri, C., 2017. A mangrove forest map of China in 2015: analysis of time series Landsat 7/8 and Sentinel-1A imagery in Google Earth Engine cloud computing platform. *ISPRS-J. Photogramm. Remote Sens.* 131, 104–120.
- Deegan, L.A., Hughes, J.E., Rountree, R.A., 2000. Salt marsh ecosystem support of marine transient species. In: Weinstein, M.P., Kreger, D.A. (Eds.), *Concepts and Controversies in Tidal Marsh Ecology*. Kluwer Academic, Dordrecht, pp. 333–365.
- Dhanjal-Adams, K.L., Hanson, J.O., Murray, N.J., Phinn, S.R., Wingate, V.R., Mustin, K., Lee, J.R., Allan, J.R., Cappadonna, J.L., Studds, C.E., Clemens, R., Roelfsema, C.M., Fuller, R.A., 2016. The distribution and protection of intertidal habitats in Australia. *Emu-Austral. Ornithol.* 116, 208–214.
- Donchyts, G., Baart, F., Winsemius, H., Gorelick, N., Kwadijk, J., Van De Giesen, N., 2016. Earth's surface water change over the past 30 years. *Nat. Clim. Chang.* 6, 810–813.
- Dong, J., Xiao, X., Menarguez, M.A., Zhang, G., Qin, Y., Thau, D., Biradar, C., Moore 3rd, B., 2016. Mapping paddy rice planting area in northeastern Asia with Landsat 8 images, phenology-based algorithm and Google Earth Engine. *Remote Sens. Environ.* 185, 142–154.
- FAO, 2016. *Fishery and Aquaculture Statistics*, 2016. Food and Agriculture Organization of the United Nations, Roma, Italy.

- Ghosh, S., Mishra, D.R., Gitelson, A.A., 2016. Long-term monitoring of biophysical characteristics of tidal wetlands in the northern Gulf of Mexico-A methodological approach using MODIS. *Remote Sens. Environ.* 173, 39–58.
- Gong, P., Liu, H., Zhang, M., Li, C., Wang, J., Huang, H., Clinton, N., Ji, L., Li, W., Bai, Y., Chen, B., Xu, B., Zhu, Z., Yuan, C., Ping Suen, H., Guo, J., Xu, N., Li, W., Zhao, Y., Yang, J., Yu, C., Wang, X., Fu, H., Yu, L., Dronova, I., Hui, F., Cheng, X., Shi, X., Xiao, F., Liu, Q., Song, L., 2019. Stable classification with limited sample: transferring a 30-m resolution sample set collected in 2015 to mapping 10-m resolution global land cover in 2017. *Sci. Bull.* 64, 370–373.
- Gong, Z., Wang, Q., Guan, H., Zhou, D., Zhang, L., Jing, R., Wang, X., Li, Z., 2020. Extracting tidal creek features in a heterogeneous background using Sentinel-2 imagery: a case study in the Yellow River Delta, China. *Int. J. Remote Sens.* 41, 3653–3676.
- Guo, Q., Pu, R., Tapley, K., Cheng, J., Li, J., Jiao, T., 2019. Impacts of coastal development strategies on long-term coastline changes: a comparison between Tampa Bay, USA and Xiangshan Harbor, China. *Papers App. Geol.* 5 (1–2), 126–139.
- Han, Q., Niu, Z., Wu, M., Wang, J., 2019. Remote-sensing monitoring and analysis of China intertidal zone changes based on tidal correction. *Chin. Sci. Bull.* 64, 456–473.
- Hou, X., Wu, T., Hou, W., Chen, Q., Wang, Y., Yu, L., 2016. Characteristics of coastline changes in mainland China since the early 1940s. *Sci. China-Earth Sci.* 59, 1791–1802.
- Hu, C., Carder, K.L., Muller-Karger, F.E., 2000. Atmospheric correction of SeaWiFS imagery over turbid coastal waters: a practical method. *Remote Sens. Environ.* 74, 195–206.
- Huete, A., Liu, H., Batchily, K., van Leeuwen, W., 1997. A comparison of vegetation indices over a global set of TM images for EOS-MODIS. *Remote Sens. Environ.* 59 (3), 440–451.
- Jia, Wang, Mao, Zhang, 2019. A New Vegetation Index to Detect Periodically Submerged Mangrove Forest Using Single-Tide Sentinel-2 Imagery. *Remote Sens.* 11.
- Jia, M., Wang, Z., Zhang, Y., Mao, D., Wang, C., 2018. Monitoring loss and recovery of mangrove forests during 42 years: the achievements of mangrove conservation in China. *Int. J. Appl. Earth Obs. Geoinf.* 73, 535–545.
- Jiang, Y., Zhang, J., Chen, K., Xue, X., Michael, A.U., 2019. Moving towards a systematic marine eco-compensation mechanism in China: policy, practice and strategy. *Ocean Coast. Manag.* 169, 10–19.
- Jorgenson, M., Brown, J., 2005. Classification of the Alaskan Beaufort Sea coast and estimation of carbon and sediment inputs from coastal erosion. *Geo-Mar. Lett.* 25, 69–80.
- Khan, M.J.U., Ansary, M.D.N., Durand, F., Testut, L., Ishaque, M., Calmant, S., Krien, Y., Islam, A.K.M.S., Papa, F., 2019. High-resolution intertidal topography from Sentinel-2 multi-spectral imagery: synergy between remote sensing and numerical modeling. *Remote Sens.* 11.
- Li, H., Jia, M., Zhang, R., Ren, Y., Wen, X., 2019. Incorporating the plant Phenological trajectory into mangrove species mapping with dense time series Sentinel-2 imagery and the Google earth engine platform. *Remote Sens.* 11.
- Liu, M., Li, H., Li, L., Man, W., Jia, M., Wang, Z., Lu, C., 2017. Monitoring the invasion of *Spartina alterniflora* using multi-source high-resolution imagery in the Zhejiang estuary, China. *Remote Sens.* 9.
- Ma, Z., Melville, D.S., Liu, J., Chen, Y., Yang, H., Ren, W., Zhang, Z., Piersma, T., Li, B., 2014. Rethinking China's new great wall. *Science* 346, 912–914.
- Mao, D., Wang, Z., Wu, J., Wu, B., Zeng, Y., Song, K., Yi, K., Luo, L., 2018. China's wetlands loss to urban expansion. *Land Degrad. Dev.* 29, 2644–2657.
- Mao, D., Liu, M., Wang, Z., Li, L., Man, W., Jia, M., Zhang, Y., 2019. Rapid invasion of *Spartina alterniflora* in the coastal zone of mainland China: spatiotemporal patterns and human prevention. *Sensors* 19, 2308.
- McFeeters, S.K., 1996. The use of the Normalized Difference Water Index (NDWI) in the delineation of open water features. *Int. J. Remote Sens.* 17, 1425–1432.
- Meng, W., Hu, B., He, M., Liu, B., Mo, X., Li, H., Wang, Z., Zhang, Y., 2017. Temporal-spatial variations and driving factors analysis of coastal reclamation in China. *Estuar. Coast. Shelf Sci.* 191, 39–49.
- Mitch, W., Gosselink, J., 2007. Wetlands. Hoboken. Wiley, New Jersey, p. 574.
- Murray, N., Phinn, S., Clemens, R., Roelfsema, C., Fuller, R., 2012. Continental scale mapping of tidal flats across East Asia using the Landsat archive. *Remote Sens.* 4, 3417–3426.
- Murray, N.J., Clemens, R.S., Phinn, S.R., Possingham, H.P., Fuller, R.A., 2014. Tracking the rapid loss of tidal wetlands in the Yellow Sea. *Front. Ecol. Environ.* 12, 267–272.
- Murray, N.J., Ma, Z., Fuller, R.A., 2015. Tidal flats of the Yellow Sea: a review of ecosystem status and anthropogenic threats. *Austral Ecol.* 40, 472–481.
- Murray, N.J., Phinn, S.R., DeWitt, M., Ferrari, R., Johnston, R., Lyons, M.B., Clinton, N., Thau, D., Fuller, R.A., 2019. The global distribution and trajectory of tidal flats. *Nature* 565, 222–225.
- Otsu, N., 1979. A threshold selection method from gray-level histograms. *IEEE Trans. Syst. Man Cybern.* 9, 62–66.
- Ren, C., Wang, Z., Zhang, Y., Zhang, B., Chen, L., Xi, Y., Xiao, X., Doughty, R.B., Liu, M., Jia, M., Mao, D., Song, K., 2019. Rapid expansion of coastal aquaculture ponds in China from Landsat observations during 1984–2016. *Int. J. Appl. Earth Obs. Geoinf.* 82, 101902.
- Rogers, A.S., Kearney, M.S., 2003. Reducing signature variability in unmixing coastal marsh Thematic Mapper scenes using spectral indices. *Int. J. Remote Sens.* 25, 2317–2335.
- Sagar, S., Roberts, D., Bala, B., Lymburner, L., 2017. Extracting the intertidal extent and topography of the Australian coastline from a 28 year time series of Landsat observations. *Remote Sens. Environ.* 195, 153–169.
- Singh, K.V., Setia, R., Sahoo, S., Prasad, A., Pateriya, B., 2015. Evaluation of NDWI and MNDWI for assessment of waterlogging by integrating digital elevation model and groundwater level. *Geocarto Int.* 30, 650–661.
- Tian, J., Wang, L., Yin, D., Li, X., Diao, C., Gong, H., Shi, C., Menenti, M., Ge, Y., Nie, S., Ou, Y., Song, X., Liu, X., 2020. Development of spectral-phenological features for deep learning to understand *Spartina alterniflora* invasion. *Remote Sens. Environ.* 242.
- Tiner, R.W., 2013. Tidal Wetlands Primer: An Introduction to their Ecology, Natural History, Status, and Conservation. University of Massachusetts Press.
- Tragano, D., Aggarwal, B., Poursanidis, D., Topouzelis, K., Chrysoulakis, N., Reinartz, P., 2018. Towards global-scale seagrass mapping and monitoring using Sentinel-2 on Google Earth Engine: the case study of the Aegean and Ionian seas. *Remote Sens.* 10, 1227.
- Tucker, C.J., 1979. Red and photographic infrared linear combinations for monitoring vegetation. *Remote Sens. Environ.* 8, 127–150.
- United Nations (UN), 2015. Transforming Our World: The 2030 Agenda for Sustainable Development Annex/RES/70/1. [https://sustainabledevelopment.un.org/post\\_2015/transformingourworld](https://sustainabledevelopment.un.org/post_2015/transformingourworld).
- Wang, X., Xiao, X., Zou, Z., Chen, B., Ma, J., Dong, J., Doughty, R.B., Zhong, Q., Qin, Y., Dai, S., Li, X., Zhao, B., Li, B., 2020a. Tracking annual changes of coastal tidal flats in China during 1986–2016 through analyses of Landsat images with Google Earth Engine. *Remote Sens. Environ.* 238, 110987.
- Wang, X., Xiao, X., Zou, Z., Hou, L., Qin, Y., Dong, J., Doughty, R.B., Chen, B., Zhang, X., Chen, Y., Ma, J., Zhao, B., Li, B., 2020b. Mapping coastal wetlands of China using time series Landsat images in 2018 and Google Earth Engine. *ISPRS-J. Photogramm. Remote Sens.* 163, 312–326.
- Wicaksono, A., Wicaksono, P., 2019. Geometric Accuracy Assessment for Shoreline Derived from NDWI, MNDWI, and AWEI Transformation on Various Coastal Physical Typology in Jepara Regency using Landsat 8 OLI Imagery in 2018. *Geoplanning* 6.
- Xu, H., 2006. Modification of normalised difference water index (NDWI) to enhance open water features in remotely sensed imagery. *Int. J. Remote Sens.* 27, 3025–3033.
- Xu, N., Gong, P., 2018. Significant coastline changes in China during 1991–2015 tracked by Landsat data. *Sci. Bull.* 63, 883–886.
- Yang, Y., Liu, Y., Zhou, M., Zhang, S., Zhan, W., Sun, C., Duan, Y., 2015. Landsat 8 OLI image based terrestrial water extraction from heterogeneous backgrounds using a reflectance homogenization approach. *Remote Sens. Environ.* 171, 14–32.
- Zhang, H., Jiang, Q., Xu, J., 2013. Coasline Extraction Using Support Vector Machine from Remote Sensing Image. *J. Multimed.* 8, 175–182.
- Zhang, D., Liu, G., Hu, W., 2019. Mapping Tidal Flats with Landsat 8 Images and Google Earth Engine: a case study of the China's Eastern Coastal Zone circa 2015. *Remote Sens.* 11, 924.
- Zhao, C., Qin, C.-Z., Teng, J., 2020b. Mapping large-area tidal flats without the dependence on tidal elevations: a case study of Southern China. *ISPRS-J. Photogramm. Remote Sens.* 159, 256–270.
- Zhong, L., Hu, L., Zhou, H., 2019. Deep learning based multi-temporal crop classification. *Remote Sens. Environ.* 221, 430–443.